Failure mechanism of deformed concrete tunnel linings with a cave

背面空洞がある変形したコンクリートトンネル覆工の破壊メカニズム

Wei He* and Zhishen Wu**
何 偉　呉 智深

*Dr. Candidate of Eng., Dept. of Urban & Civil Eng., Ibaraki University
(4-12-1, Nakanarusawa-cho, Hitachi, Ibaraki 316-8511, Japan)
**Dr. of Eng., Professor, Dept. of Urban & Civil Eng., Ibaraki University
(4-12-1, Nakanarusawa-cho, Hitachi, Ibaraki 316-8511, Japan)

This paper presents different failure modes of concrete tunnel linings with a cave. The compressive failure mechanism is explained using the concept of the compressive softening hinge. It is found that the structural dominant failure is varied with the cave range. With small cave range, the structural dominant failure is compressive failure; while with large cave range, it is tensile failure. Furthermore, the compressive yielding zones and their locations have a dominated influence on the load-carrying capacity of tunnels. In addition, the compressive behavior of concrete increases the structural ductility, and the multiple cracking propagations are responsible for the structural brittleness.

Key Words: cave, compressive softening hinge, compressive failure, tensile failure

1. Introduction

There are many concrete tunnels in modern highways and railways. Recently, the issue on assessments and rehabilitations of deformed and deteriorating tunnels has become a big concern in tunnel and structural engineering. To develop the rational design and assessment approaches of concrete tunnel linings, some researchers have done fruitful work on identification of failure modes of concrete tunnel linings. Asakura et al. (1994, 1998)[1),2)] carried out a series of experiments based on 1/30, 1/20 and 1/3 scale model of real concrete tunnel linings. Through his experimental studies, some typical cracking propagation patterns and concrete compressive failure modes have been identified. Yin et al. (2001)[3)] simulated the tunnel behavior using smeared crack model. In his study, the cracking behavior of plain concrete tunnel linings, including crack occurrence, crack propagation, and the factors affecting the cracking behavior and the structural responses, is clarified. He et al. (2003)[4)] pointed out that the compressive failure of concrete is an important failure mode of tunnel linings. According to the study, the structural load-carrying capacity as well as the deformation behavior clearly depends on the compressive behavior of concrete. Especially, in his studies, the compressive strain softening behavior of concrete has a big effect on the structural responses of tunnel linings. However, due to the complexity of surrounding media outside concrete tunnel linings, the failure modes and failure processes of concrete tunnels are obviously varied with the external boundary conditions. Of all the issues, the failure mechanism is still not very clear.

Green Tuff region, which consists of soft rocks generated during Neogene Period, are widely distributed in Japan. As one type of geologic defects and as a special case of external boundary conditions, the caves behind the tunnel lining are often disadvantageous to the normal service of tunnels. Therefore, the influence of caves on the failure modes of tunnels is clarified in this paper. For example, due to the variation of the cave range, concrete tunnels exhibit different failure modes, such as compressive failure or tensile failure. To determine the effect of the location and the scale of concrete compressive softening zone on the load-carrying capacity and deformation behavior of concrete tunnels, this paper specifies different compressive softening patterns of concrete. It is helpful to understand the structural responses of deformed tunnels. For the convenience of comparison with available experimental results, the tunnel subjected to plastic ground pressure is studied. For the details of plastic ground pressure, refer to He et al. (2004)[5)].

The layout of this paper is as follows. Firstly, the experimental setup and experimental results are briefly reviewed. Secondly, based on the parabolic compressive strain softening model as

well as the linear tensile strain softening model, the simulation model is introduced. Finally, the failure mechanism of concrete tunnels with varied range of the cave, which is behind the concrete tunnel linings in the ceiling area, is studied.

2. Experimental Review

To evaluate the structural performance of concrete tunnel linings, a series of model experiments of tunnel linings was carried out by *RTRI* (Railway Technical Research Institute of Japan). The experimental setup and experimental results are shown as follows[2].

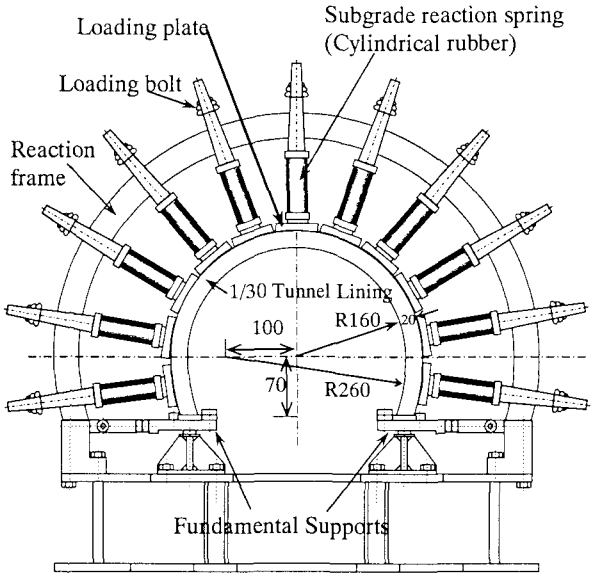

Fig.1 Outline of the 1/30 scale model for double track tunnels (unit: mm)

2.1 Experimental Setup

A 1/30 scale model for double track tunnels is shown in Fig.1. The test setup consists of a loading device, a reaction frame, and fundamental supports, etc. The load reactor includes a loading plate, a cylindrical spring made up of hard rubber, and double threaded screw bolts. Eleven independent load applicators are available in the normal direction through the simulated tunnel surface. The bolts are double screw structures, and the inner side allows for the compression and release of the cylindrical springs. The parts at loading portion are made up of steel cylinder instead of cylindrical spring and it can directly cause the displacement to the lining model by rotating the outer bolt. Furthermore, at all points except the loading points, an elastic reaction can be introduced by fixing the outer bolt to the reaction frame. The horizontal direction of the tunnel lining at the foot is constrained by springs as shown in Fig.2. In the present study, the external load is applied at the outside crown symmetrically.

The material properties of experiments are as follows: concrete Young's modulus E_c = 1.5×10^4 MPa, Poisson ratio ν = 0.15, tensile strength f_t = 2.0 MPa, compressive strength f'_c = 21.0 MPa, soil stiffness K_{soil} = 110 N/mm, and the stiffness of foot constraining spring K_{foot} = 400 N/mm. All the material properties of concrete, soil stiffness and other parameters are from the experimental tests.

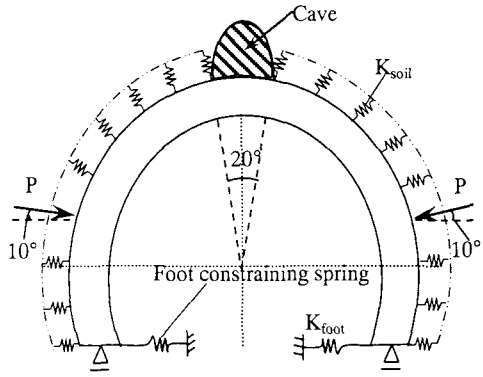

(a) Experimental case 1

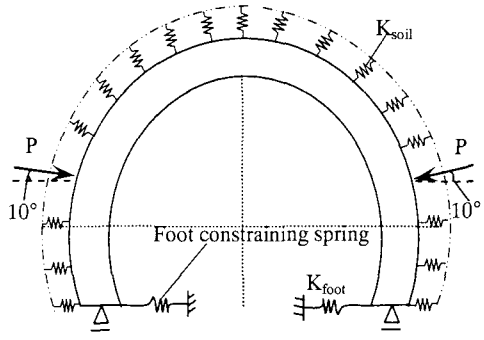

(b) Experimental case 2

Fig.2 Experimental cases

2.2 Experimental Results

Two experimental cases are studied in the present paper. The concentrated loads were acted at the outside sidewalls of the concrete tunnel symmetrically, with load direction inclined to the horizontal with angle 10°. To investigate the influence of the cave behind tunnel linings on the structural behavior, one experimental case comprised of a cave whose range is 20°, and the other experimental case contained no cave are presented, as shown in Fig.2. Load-displacement responses are shown in Fig.3. The displacement in the experimental load-displacement curves denotes the displacement at load point.

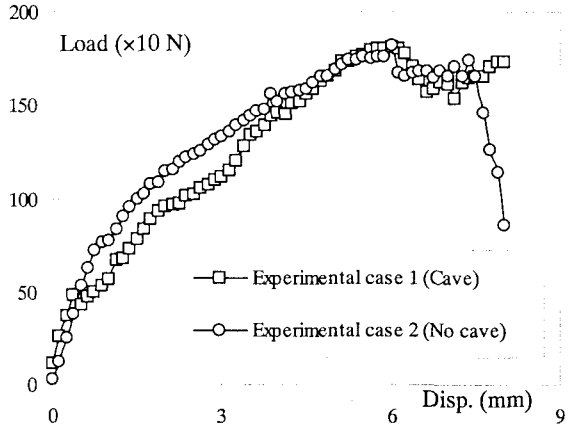

Fig.3 Load-displacement curve (experimental)

3. Material and Computational Models

3.1 Material Model for Concrete

The material model for concrete is based on the total strain, namely the 'Total Strain Rotating Crack Model', which describes the compressive and tensile behaviors of a material with one co-rotational stress-strain relationship. It is developed based on the Modified Compression Field Theory (MCFT), proposed originally by Vecchio and Collins (1986)[6]. The three-dimensional extension to this theory is developed further by Selby and Vecchio (1993)[7], and has been enhanced by Feenstra et al. (1998)[8]. The practical use of a rotating stress-strain relation requires principal stress and principal strain to be coaxial. It has been known that this coaxiality can be achieved via an implicit shear term in the rotating principal 1, 2 reference frame. Moreover, the total strain rotating crack model can be derived as a special case of the decomposed multi-directional model assuming a zero inter-crack threshold angle, so that a new crack under slightly different angle is initiated in each step while the previous cracks unload elastically.

a) Compressive Behavior for Concrete

For the compressive behavior of concrete, the parabolic compressive softening model based on total strain is used in the present paper, as shown in Fig.4. When concrete is loaded in compression, the response is assumed linear until one third of peak load. It can be expressed as follows:

$$\sigma_3 = E_c \varepsilon_3, \quad \text{if } 0 \le \varepsilon_3 < \varepsilon_{ce} \tag{1}$$

where E_c is the concrete Young's initial modulus, and ε_{ce} is

$$\varepsilon_{ce} = \frac{1}{3}\left(\frac{f_c'}{E_c}\right) \tag{2}$$

in which f'_c is the concrete compressive strength.

In the compressive regime, the response is typically characterized by stress hardening followed by strain softening beyond the maximum attainable stress f'_c. For concrete in the direction of the largest principal compressive strain (ε_3) with compressive hardening and softening, the stress-strain relation of concrete subjected to the compression is usually expressed mathematically by a parabolic curve (see Matthias et. al., 2002)[9]:

$$\sigma_3 = \begin{cases} \dfrac{f_c'}{3}\left[1 + 4\dfrac{\varepsilon_3}{\varepsilon_{c0}} - 2\left(\dfrac{\varepsilon_3}{\varepsilon_{c0}}\right)^2\right] & \text{if } \varepsilon_{ce} \le \varepsilon_3 < \varepsilon_{c0} \\ f_c'\left[1 - \left(\dfrac{\varepsilon_3 - \varepsilon_{c0}}{\varepsilon_{cu} - \varepsilon_{c0}}\right)^2\right] & \text{if } \varepsilon_{c0} \le \varepsilon_3 \le \varepsilon_{cu} \end{cases} \tag{3}$$

where

$$\varepsilon_{c0} = \frac{2f_c'}{E_c} \tag{4}$$

and

$$\varepsilon_{cu} = \frac{3G_c}{2f_c'h} + \varepsilon_{c0} \tag{5}$$

with the concrete compressive fracture energy G_c and characteristic crack length h based on the element geometry. For planar elements, h is the square root of the element area.

When the stress state is in compressive-tensile condition, the major principal tensile strain, which is perpendicular to the compressive direction, may decrease the maximum attainable compressive stress f_{3max}. The reduction in the maximum attainable compressive stress f_{3max}, as a function of the coexisting transverse tensile strain ε_1, typically represents a significant softening effect. It can be evaluated by the equation (see Vecchio et. al., 1986)[6]:

$$f_{3\max} = \frac{f'_c}{0.8 - (0.34\dfrac{\varepsilon_1}{\varepsilon_0})} \tag{6}$$

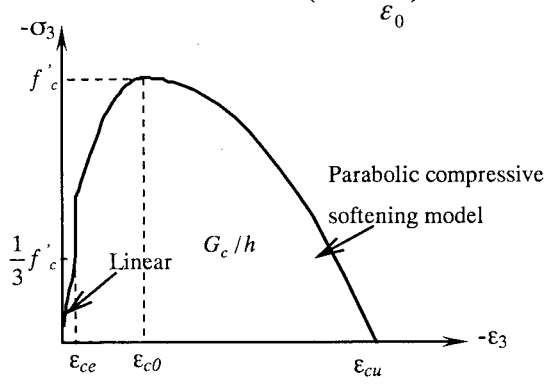

Fig.4 Concrete in compression

b) Tensile Behavior for Concrete

The tensile behavior of concrete can be modeled using different approaches. For the total strain crack model, the conventional linear softening stress-strain relation based on Mode-I fracture energy is adopted in this paper, as shown in Fig.5. Conditions of equilibrium and compatibility were treated in terms of average stresses and average strains. Local stress conditions at crack locations were also considered. For the details, refer to Feenstra et al. (1998)[8].

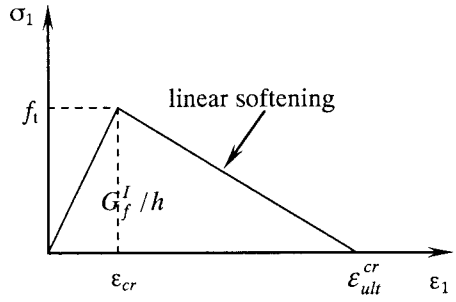

Fig.5 Concrete in tension

In Fig.5, $\varepsilon^{cr}{}_{ult}$ is given by (see Matthias et. al., 2002)[9]

$$\varepsilon_{ult}^{cr} = G^{I}{}_{f} / f_t h \tag{7}$$

in which $G^{I}{}_{f}$ is tensile fracture energy of concrete, f_t is tensile strength of concrete, and h is the square root of the element area.

c) Material Stiffness Matrix

The material stiffness matrix $\boldsymbol{D}$ that relates stresses $\{\boldsymbol{\sigma}\}$ to strains $\{\boldsymbol{\varepsilon}\}$ is given by

$$\{\boldsymbol{\sigma}\} = \boldsymbol{D}\{\boldsymbol{\varepsilon}\} \tag{8}$$

where $\{\boldsymbol{\sigma}\} = [\sigma_x \sigma_y \sigma_z \tau_{xy} \tau_{yz} \tau_{xz}]$, and $\{\boldsymbol{\varepsilon}\} = [\varepsilon_x \varepsilon_y \varepsilon_z \gamma_{xy} \gamma_{yz} \gamma_{xz}]$.

The form of the matrix $\boldsymbol{D}$ will depend on the type of nonlinear solution algorithm employed. The formulations adopt a secant-stiffness approach. This approach is according to the stiffness of an orthotropic material with zero Poisson's ratio in all directions. Moreover, the material stiffness $\boldsymbol{D}_{secant}$ is evaluated with respect to the principal axes systems (1, 2, 3). And then it must be transformed to the global coordinates. It can be written as

$$\boldsymbol{D} = \boldsymbol{T}^{T}\boldsymbol{D}_{secant}\boldsymbol{T} \tag{9}$$

where $\boldsymbol{T}$ is the transformation matrix.

3.2 Structural Model

The concrete tunnel is discretized by 4-node quadrilateral plane stress elements as shown in Fig.6. 2×2 Gaussian integration is adopted. The line interface element is used to simulate soil constraint outside the concrete tunnel.

The loading conditions include soil pressure and plastic ground pressure. Soil pressure is considered as a distributed load, while the plastic ground pressure is considered as symmetrical concentrated loads.

4. Numerical Simulations

The analysis is mainly concerned with the failure modes of the concrete tunnel varied with the cave range. In addition, the load-carrying capacity and deformation behavior of the concrete tunnel are also studied.

The material properties of simulations are as follows: concrete Young's modulus E_c = 1.5×10^4 MPa, Poisson ratio ν = 0.15, tensile strength f_t = 2.0 MPa, tensile fracture energy G_f^I = 0.1 N/mm, compressive strength f'_c = 14.0 MPa which is identified from FEM calculation, concrete compressive fracture energy G_c = 100 N/mm, soil stiffness K_{soil} = 110 N/mm, and the stiffness of foot constraining spring K_{foot} = 400 N/mm.

In the experiment, only the cave range of 20° was considered. However, the cave range is different in practical engineering applications. Therefore, except for the experimental case of cave range of 20°, other cave ranges are also studied. For the convenience of discussion, the cave ranges are divided into two groups. One group is symmetrical cave ranges, which is symmetrical along the axis of the concrete tunnel lining; the other group is unsymmetrical cave ranges, as shown in Fig.6. As two extreme cases of cave ranges, full cave denotes there is no soil constraint around the tunnel lining, while the cave range of 0° denotes there is no cave behind the tunnel lining.

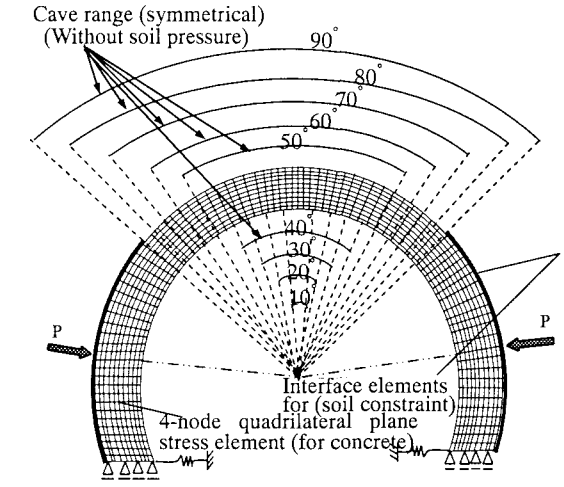

(a) Symmetrical cave

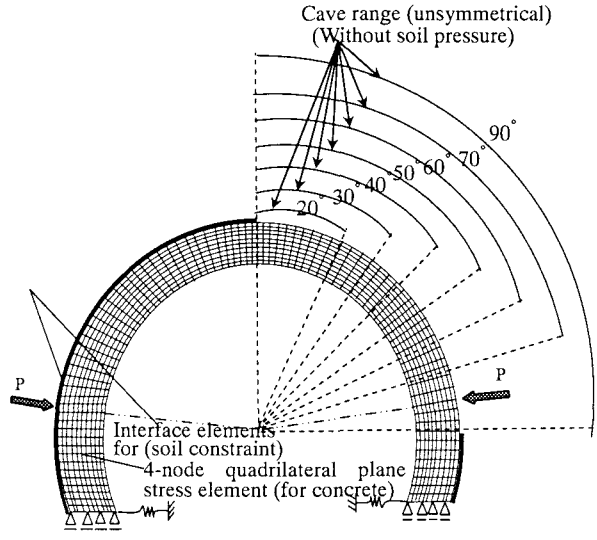

(b) Unsymmetrical cave

10° (20°, 30°, etc.) denotes the range of cave behind the tunnel lining.

Fig.6 Structural model for FE analysis and different cave ranges

4.1 Symmetrical Cave

Fig.7 shows the initial stiffness of the tunnel without cave is larger than that of the tunnel with the cave. It is due to existence of the cave, which allows larger deformation toward the ceiling area of the tunnel; and hence the initial structural stiffness decreased. The numerical results also show that the tunnel

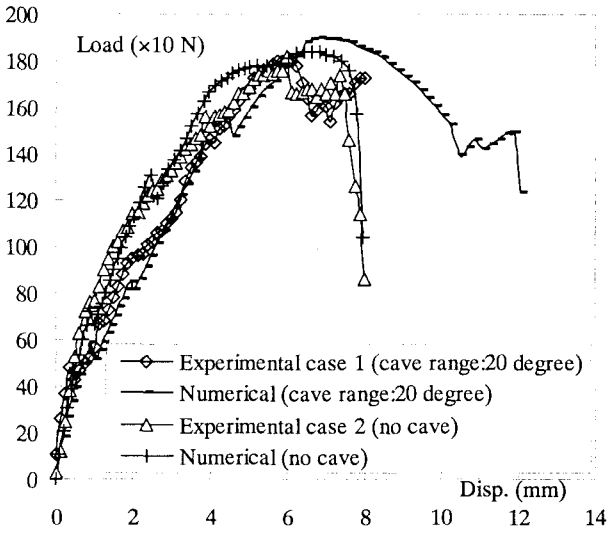

Fig.7 Load-displacement response: comparison between experimental results and FE analysis (symmetrical caves)

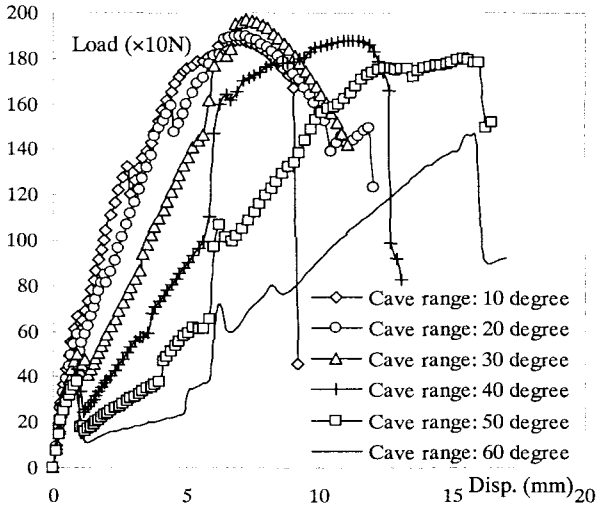

(a) Symmetrical cave case I

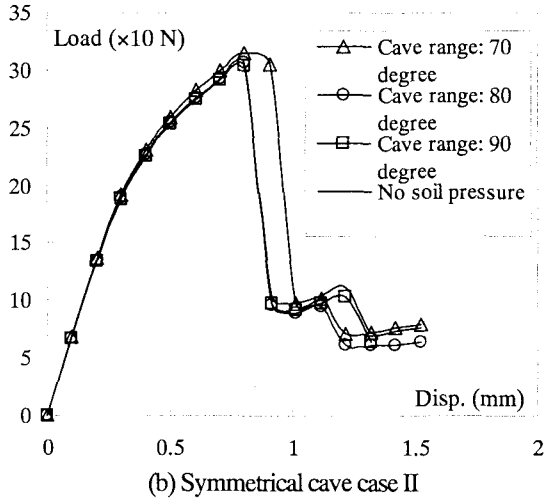

(b) Symmetrical cave case II

Fig.8 Load-displacement response of different cave ranges (symmetrical caves)

without cave exhibits more brittle behavior after the structure reaches its load-carrying capacity. The reason is the propagation of the multiple cracks.

In Fig.8 (a), the structural load-carrying capacity exhibits no big difference with in the cave ranges from 10° to 50°. When the cave range increases to 70°, the structural load-carrying capacity is quite low, as shown in Fig.8 (b).

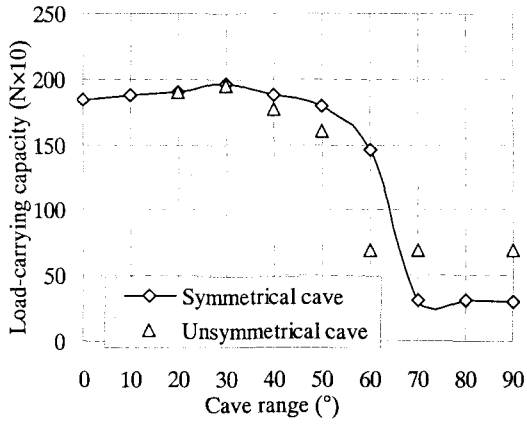

(a) Load-carrying capacity of different cave ranges

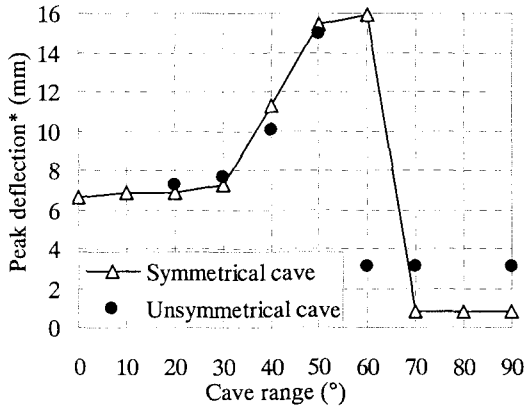

(*: Peak deflection corresponding to the load-carrying capacity)

(b) Peak deflection of different cave ranges

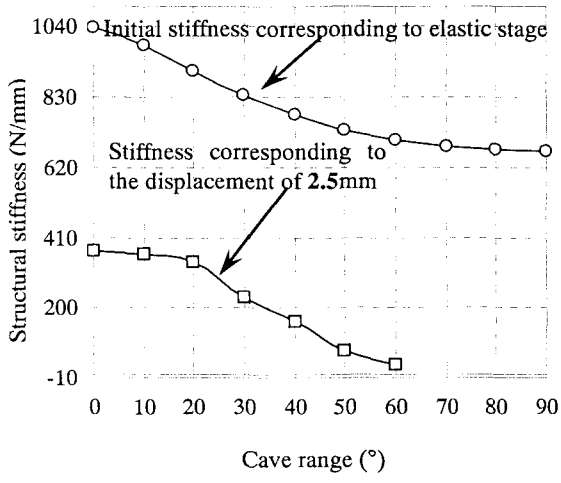

(c) Structural stiffness of different cave ranges

(The cave range of 0° denotes there is no cave)

Fig.9 Structural response of different cave ranges

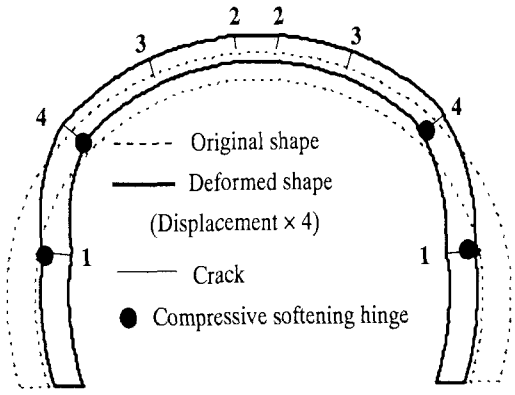

(a) Deformed shape (No cave)

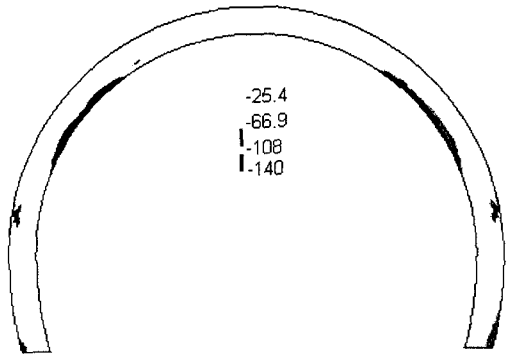

(b) Compressive stress σ_2 ($\times 10^5$ Pa), no cave

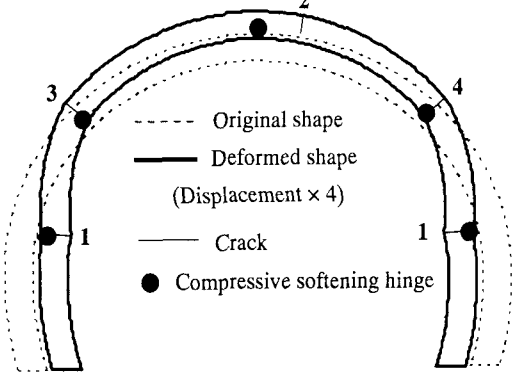

(c) Deformed shape (Cave range: 20°)

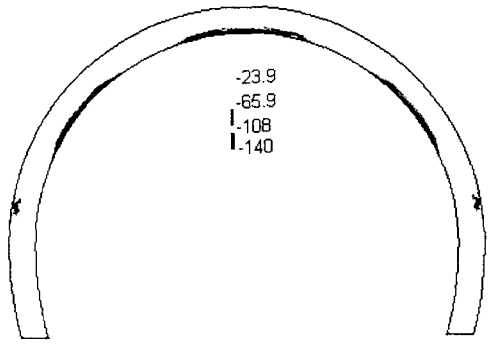

(d) Compressive stress σ_2 ($\times 10^5$ Pa), cave range: 20°

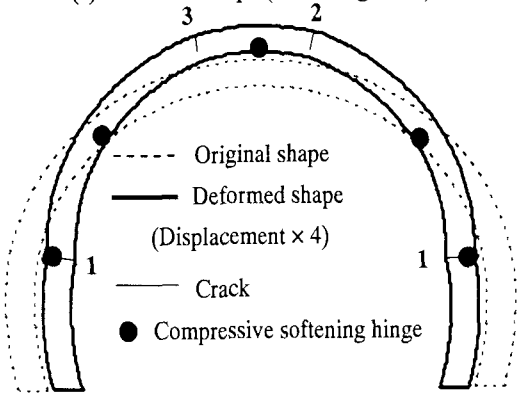

(e) Deformed shape (Cave range: 30°)

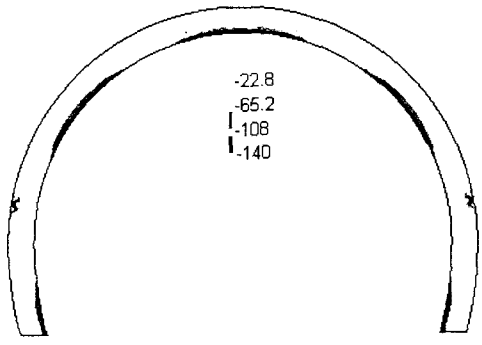

(f) Compressive stress σ_2 ($\times 10^5$ Pa), cave range: 30°

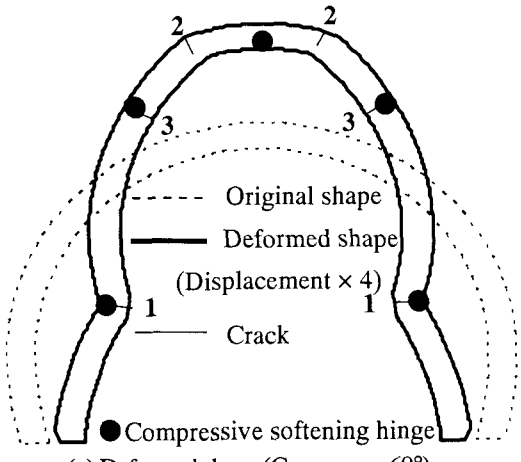

(g) Deformed shape (Cave range: 60°)

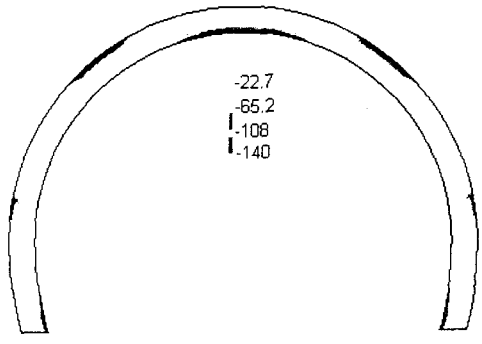

(h) Compressive stress σ_2 ($\times 10^5$ Pa), cave range: 60°

1, 2, 3: Sequence of cracking occurrence

Fig.10 Compressive failure modes of different cave ranges (symmetrical cave)

In Fig.9 (a), it is interesting to find that the structural load-carrying capacity increases with in the cave ranges from 0 to 30°. Comparing the case of no cave with that of the cave range of 20°, the load-carrying capacity of the tunnel with the cave range of 20° is higher, because one more compressive softening hinge occurred in the crown of the tunnel (see Fig.10 (c)). In comparison of the cave range of 20° with that of 30°, the load-carrying capacity of the later is higher, due to the fact that the compressive softening zones are larger in the case of the cave range of 30° (see Fig.10 (d) and (f)), although the total number of the compressive softening hinges and the locations of the compressive softening hinges are the same in both cases. In Fig.9 (b), the peak deflection, which is corresponding to the load-carrying capacity, increases with in the cave ranges from 0 to 60°; while the peak deflection decreases at 60°. It shows the compressive behavior of concrete has dominant influence on the structural deformation, because the compressive failure is dominant failure with in the cave ranges from 0 to 60°. The numerical results also show that the structural stiffness decreases with the increase of the cave range, as shown in of Fig.9 (c).

From the cracking pattern of the tunnel without cave (see Fig.10 (a)), two cracks occurred near the crown (outside) immediately after cracking initiation in the direction of loading point (inside); and then another two cracks, the sequence of which is named '3', initiated at the sidewalls of the tunnel. Although compressive softening hinges have developed, the structure lost its strength quickly, due to the occurrence of the last two cracks named '4'. The compressive softening hinge involves strain softening in compression after compressive yielding of concrete, which is different from the conventional plastic hinge.

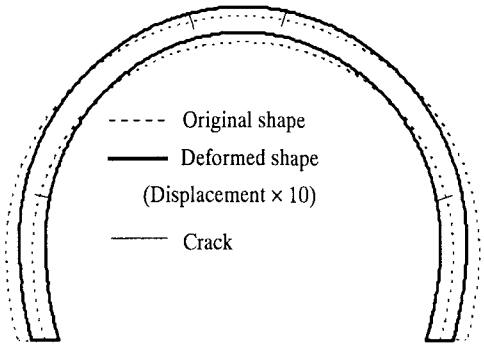

(a) Deformed shape (cave range: 70°)

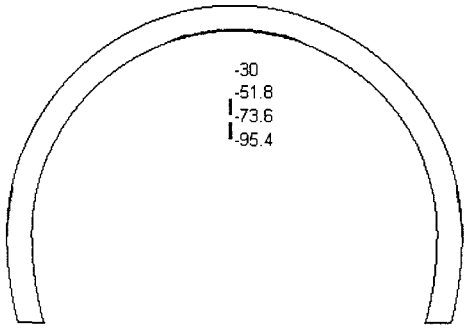

(b) Compressive stress σ_2 ($\times 10^5$ Pa), cave range: 70°

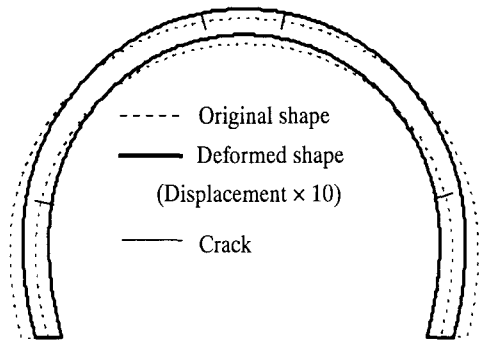

(c) Deformed shape (No soil pressure)

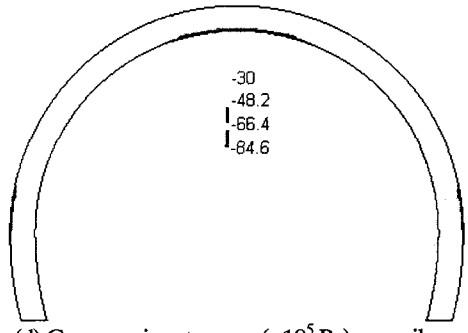

(d) Compressive stress σ_2 ($\times 10^5$ Pa), no soil pressure

Fig.11 Tensile failure modes of different cave ranges (symmetrical cave)

As expected, the structural load-carrying capacity decreases with the cave ranges from 30° to 90°, as shown in Fig.9 (a). This is due to the decrease of the compressive yielding zones with the increase of cave range. It is notable that the compressive softening hinges namely '3' occurred at the outside sidewalls, in the case of the cave range of 60° (see Fig.10 (g)). In Fig.10 (e) and (g), the large deformation occurred at the crown of the liner. The reason is that the cave behind the liner allows the larger deformation toward the ceiling area of the tunnel. In real engineering applications, the large deformation of the liner makes the structure unstable. Hence, to remedy the problem caused by the cave, the countermeasure is to fill the cave using concrete or other proper material.

From numerical results in Fig.10 and Fig.11, it is found that the final failure of the tunnel is compressive failure, with in the cave ranges from 0 to 60°; while the final failure of the tunnel is tensile failure, when the cave range larger than or equal to 70°. In addition, it can be concluded that the load-carrying capacity depends on the failure mode of the tunnel. For example, when the tunnel is subjected to the tensile failure, the load-carrying capacity is lower than that of the tunnel subjected to the compressive failure.

4.2 Unsymmetrical Cave

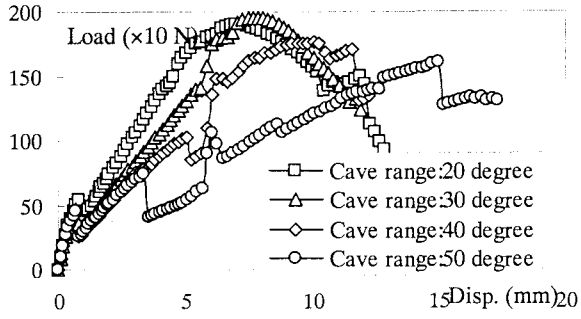

(a) Unsymmetrical cave case I

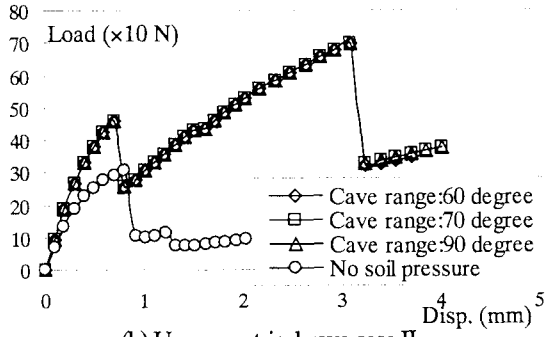

(b) Unsymmetrical cave case II

Fig.12 Load-displacement response of different cave ranges (unsymmetrical cave)

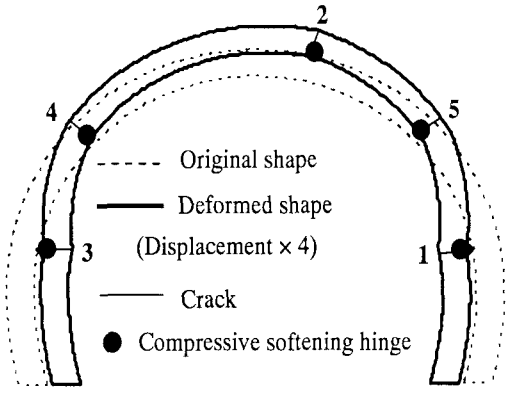

(a) Deformed shape (Cave range: 20°)

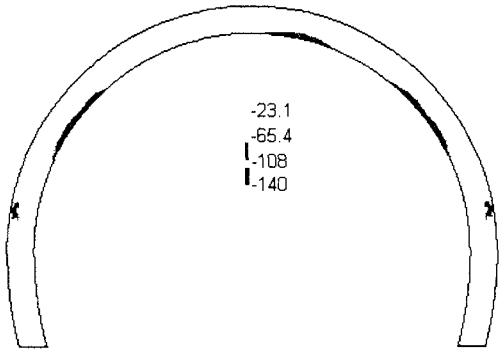

(b) Compressive stress σ_2 (×10^5 Pa), cave range: 20°

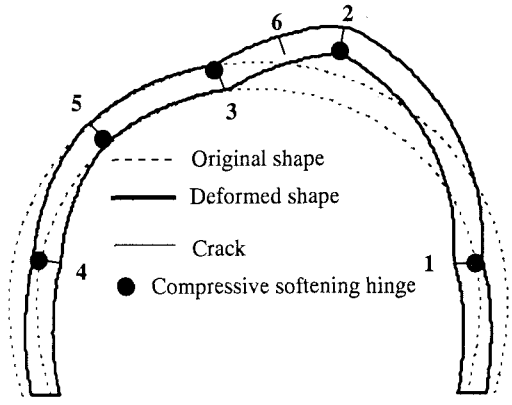

(c) Deformed shape (Cave range: 50°)

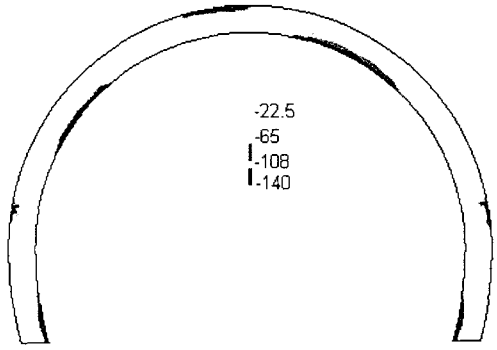

(d) Compressive stress σ_2 (×10^5 Pa), cave range: 50°

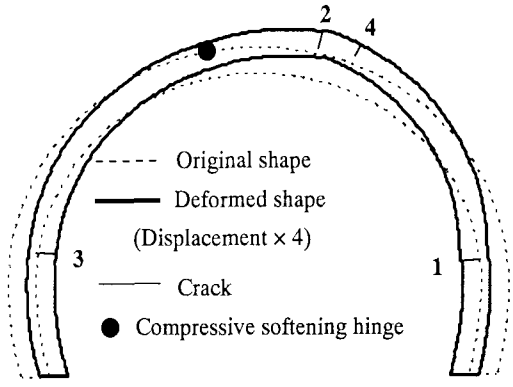

(e) Deformed shape (Cave range: 60°)

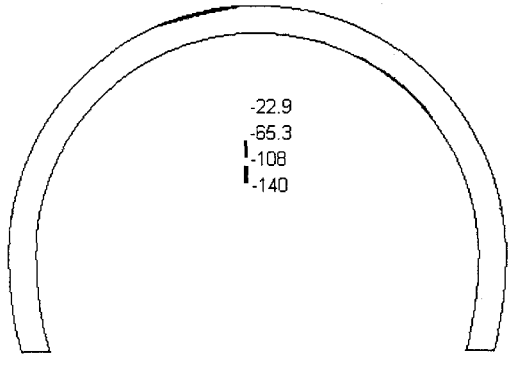

(f) Compressive stress σ_2 (×10^5 Pa), cave range: 60°

Fig.13 Failure modes of different cave ranges (unsymmetrical caves)

In the case of the unsymmetrical cave, the structural load-carrying capacity increases with cave ranges from 0 to 30°; and it decreases with cave ranges from 30° to 60°, as shown in Fig.12 As compared with the case of cave range of 20°, the load-carrying capacity of the cave range of 50° is lower, because the crack namely '6' (see Fig.13 (c)) appears which makes the tunnel lose its strength suddenly.

In Fig.12 (b), it is found that the load-carrying capacity of the cave range from 60° to 90° is almost the same; meanwhile, the load-carrying capacity of the cave range of 60° is higher than that without soil pressure, owing to the concrete compressive yielding (Fig.13 (e) and (f)). Although the load-carrying capacity of the cases with unsymmetrical cave range from 60° to 90° is higher than that of the cases with symmetrical cave range from 70° to 90°, both of their failure mode is tensile failure. As mentioned above, the large deformation occurred at crown of the tunnel as shown in Fig.13 (c) and (e), so the cave should be filled in actual applications.

5. Conclusions

In this paper, structural response of concrete tunnels with a cave is studied. The numerical simulations have been carried out to investigate the compressive and cracking behavior of 1/30 scale model of the concrete tunnel. From the studies, the following conclusions are drawn:

(1) The failure mode of concrete tunnels is varied with the cave behind the tunnel linings. In the case of symmetrical cave, the dominant failure is compressive failure with in the cave ranges from 0 to 60°. It is however of tensile failure when the cave range is larger than or equals to 70°. In the case of unsymmetrical cave, the dominant failure is compressive failure with in the cave ranges from 0 to 50°, but the final failure is tensile failure with that the cave range is larger than or equals to 60°.

(2) The compressive behavior of concrete has a dominant influence on the load-carrying capacity of tunnels. Both of the compressive yielding zones and their locations are responsible for the structural strength.

(3) The deformation of tunnels is determined by the compressive behavior as well as the cracking propagations. The structure often exhibits ductile behavior with the formation of compressive softening hinges; while the structure exhibits brittle behavior with multiple cracking propagations.

References

1) Asakura, T., Ando, T., Omata, F., Wakana, K., and Matsuura, A., Behavior of structurally defective tunnel lining and effectiveness of inner reinforcement, *Journal of Geotechnical Engineering, JSCE,* No.493, pp.89-98, 1994.
2) Asakura, T., Ando, T., and Kojima, Y., Experiments of inner reinforced tunnel linings, *QR of RTRI,* 1998.
3) Yin, J., Wu, Z.S., Asakura, T. and Ota, H., Cracking and Failure Behavior of Concrete Tunnel Lining Predicted by Smeared Crack Model, *Journal of Struc. Mech. and Earthquake Eng., JSCE*, Vol.18, No.1, 2001.1, pp.17-27.
4) He, W., Wu, Z. S., Yin, J. and Kojima, Y., Compressive failure of concrete tunnel lining simulated by different compressive models, *Journal of Applied Mechanics, JSCE,* Vol.6, pp.1207-1215, 2003.
5) He, W. and Wu, Z. S., Failure mechanism of deformed concrete tunnels under plastic ground pressure, *Journal of Applied Mechanics, JSCE,* Vol.7, pp.1203-1212, 2003.
6) Vecchio, F. J. and Collins, M. P., The modified compression field theory for reinforced concrete elements subjected to shear, *ACI Journal, Proceedings*, Vol.83, No.2, pp.219-231, 1986.
7) Selby, R. G. and Vecchio, F. J., Three-dimensional Constitutive Relations for Reinforced Concrete, *Tech. Rep. 93-02, Univ. Toronto, dept. Civil Eng., Toronto, Canada*, 1993.
8) Feenstra, P. H., Rots, J. G., Arnesen, A., Teigen, J. G., and Hoiseth, K. V., A 3D constitutive model for concrete based on a co-rotational concept, *Computational modeling of concrete structures, Proc. EURO-C,* pp.13-22, 1998.
9) Matthias Hormann, Horst Menrath, and Ekkehard Ramm, Numerical investigation of fiber reinforced polymers poststrengthened concrete slabs, *Journal of Engineering Mechanics,* Vol.128, No.5, pp.552-561, 2002.

(Received September 17, 2004)